

A Transient Thermal Model for Friction Stir Weld.

Part I: The Model

X.X. ZHANG, B.L. XIAO, and Z.Y. MA

Current analytical thermal models for friction stir welding (FSW) are mainly focused on the steady-state condition. To better understand the FSW process, we propose a transient thermal model for FSW, which considers all the periods of FSW. A temperature-dependent apparent friction coefficient solved by the inverse solution method (ISM) is used to estimate the heat generation rate. The physical reasonableness, self-consistency, and relative achievements of this model are discussed, and the relationships between the heat generation, friction coefficient, and temperature are established. The *negative feedback mechanism* and *positive feedback mechanism* are proposed for the first time and found to be the dominant factors in controlling the friction coefficient, heat generation, and in turn the temperature. Furthermore, the negative feedback mechanism is found to be the controller of the steady-state level of FSW. The validity of the proposed model is proved by applying it to FSW of the 6061-T651 and 6063-T5 aluminum alloys.

DOI: 10.1007/s11661-011-0729-5

© The Minerals, Metals & Materials Society and ASM International 2011

I. INTRODUCTION

THERMAL modeling, which can give global, intuitional, and detailed thermal information of the workpiece, has long been a standing interest in friction stir welding (FSW), a solid-state joining technique invented in 1991 by The Welding Institute (TWI) of the United Kingdom.^[1] This is because the high temperature during the FSW process changes the microstructure and mechanical properties of the welds significantly.^[2–7] It is very important to obtain temperature profiles during FSW. Although the FSW thermal cycle can be experimentally measured, it is very difficult to record the thermal history of the stir zone (SZ) because of the intense plastic deformation induced by the rotating pin in this zone. In addition, only limited temperature data can be obtained by experimental measurements.

In the past decade, several thermomechanical models based on the finite element method (FEM) and thermo-flow models based on computational fluid dynamics were established to estimate the heat flow during the FSW process.^[8–23] In addition, pure analytical thermal models^[24–32] have been also studied. No matter what kind of models are used for FSW thermal analysis, the heat generation rate is the major difficulty because of the unknown friction coefficient, which is affected by many factors. Blau's study^[33] drew our attention to the factors affecting the friction coefficient. According to his study, the main potential factors affecting the frictional coefficient in FSW are as follows: temperature, contact geometry (*i.e.*, macroscale mating of shapes and surface

roughness), relative motion (*i.e.*, magnitude of relative surface velocity), applied force (*i.e.*, magnitude of normal force), and contact compliance (*i.e.*, sliding or sticking friction conditions).

Since many potential factors could affect the friction coefficient, and the relation between them is still not very clear, it is necessary to identify the key factor(s) for a particular case, *i.e.*, FSW in the present study, for the thermal analysis. To deal with the complexity, various approximations are adopted to study the friction coefficient.^[34] By using the Coulomb friction law, Frigaard *et al.*^[25] and Song and Kovacevic^[26] took a constant friction coefficient to estimate the heat generation. Considering both sliding and sticking conditions, Schmidt *et al.*^[7,29,30] and Nandan and co-workers^[13–15] treated the friction coefficient as a function of the material shear strength and the relative speed between the tool and the workpiece. In Sluzalec's study,^[35] the first FEM study of friction welding, a temperature-dependent friction coefficient based on experimental results, was used to estimate the heat generation. In the present study, we also treat the friction coefficient as a function of temperature.

The present article aims at developing a complete description of heat generation and flow during FSW. In particular, two key developments have been made. First, the model considers the entire FSW process including plunging, first dwelling, welding, second dwelling, and cooling. Second, the friction coefficient is calculated by the inverse solution method (ISM).^[36] By doing this, it is possible to (a) predict the dynamic thermal characteristics of different FSW periods and (b) establish the relationship between the welding parameters and heat generation. (a) is studied in this article, while (b) will be described in a companion article.^[37] To demonstrate the validity of this model, it is applied to FSW of the 6061-T651 and 6063-T5 aluminum alloys. Symbols and units used in this article are defined in the Nomenclature.

X.X. ZHANG, PhD Student, and B.L. XIAO and Z.Y. MA, Professors, are with the Shenyang National Laboratory for Materials Science, Institute of Metal Research, Chinese Academy of Sciences, Shenyang 110016, P.R. China. Contact e-mail: zyma@imr.ac.cn

Manuscript submitted October 18, 2010.

Article published online May 21, 2011

II. MATHEMATICAL MODEL

A. Governing Equation for Three-Dimensional Heat Flow

The nonlinear equation for the three-dimensional heat flow of a solid in the operator notation is given by Eq. [1] based on Fourier's second law,^[38]

$$\rho(T)c(T) \frac{\partial T}{\partial t} = \nabla[\lambda(T)\nabla T] + q \quad [1]$$

in the region $\Omega = \{(x, y, z); -\frac{w}{2} \leq x \leq \frac{w}{2}, 0 \leq y \leq l, 0 \leq z \leq h\} \times [0 < t \leq t_{total}]$. In order to improve the calculation quality, temperature-dependent ρ, c , and λ are considered. The coordinate setting is shown in Figure 1.

B. Heat Generation Model

Previous research^[22] revealed that the plastic heat generation accounted for only 4.4 pct of the total heat generation for the FSW aluminum alloy. Thus, we can assume that all the heat generation results from the friction work. In this study, we further assume that the friction coefficient is a function of temperature. The reason for this assumption and its reasonable analysis will be discussed later in this article. According to these assumptions, the heat generation rate at the interface between the tool and the workpiece can be defined by

$$q = \mu(T)p \left(\frac{2\pi\omega}{60} r + \frac{v}{60} \sin \theta \right) \quad [2]$$

The details about Eq. [2], especially the temperature-dependent friction coefficient $\mu(T)$, will be discussed in Section VI.

The shoulder heat generation and the pin heat generation can be calculated by

$$Q_s = \int_0^{2\pi} \int_{R_p}^{R_s} q r dr d\theta \quad [3]$$

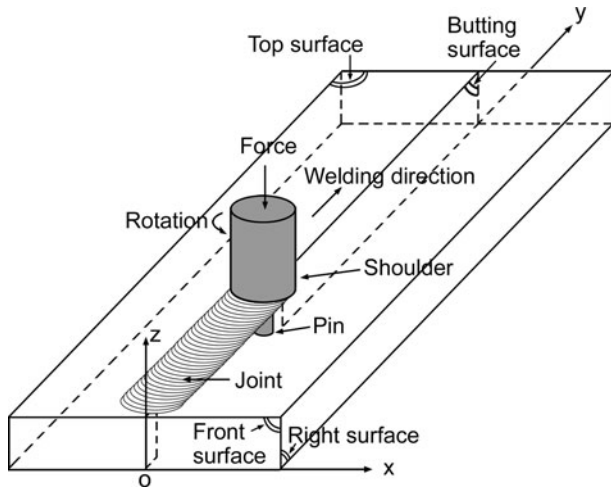


Fig. 1—Illustration of FSW and setting of coordinates and surface.

$$Q_p = \int_0^{2\pi} \int_0^{R_p} q r dr d\theta + \int_0^{2\pi} \int_0^{\beta h_p} q R_p dz d\theta \quad [4]$$

Then the total heat generation is obtained:

$$Q_{total} = Q_s + Q_p \quad [5]$$

and the pin heat generation fraction is

$$f_{pin} = \frac{Q_p}{Q_{total}} \quad [6]$$

C. Boundary Conditions

Since the heat conductivity of the workpiece (6061 aluminum alloy) is about 6 times higher than that of the tool material (M42 high speed tool steel), a significant amount of heat will be transported from the tool to the workpiece. The heat flux continuity at the tool/workpiece interface is described by^[14]

$$k \left. \frac{\partial T}{\partial z} \right|_{top} = \frac{\sqrt{(k\rho c)_W} q}{\sqrt{(k\rho c)_W} + \sqrt{(k\rho c)_T}} \quad [7]$$

where the subscripts W and T denote the workpiece and the tool, respectively.

Both convective and radiative heat transfers are considered for the heat exchange between the top, front, and back surfaces (the definition of surfaces is shown in Figure 1) of the workpiece and the surroundings:^[14]

$$-k \frac{\partial T}{\partial z} = \varepsilon\sigma(T^4 - T_a^4) + h_t(T - T_a) \quad [8]$$

Convective heat transfer between the bottom, left, and right surfaces of the workpiece and the retaining plates is given by^[14]

$$k \frac{\partial T}{\partial z} = h_b(T - T_a) \quad [9]$$

Temperatures of the surroundings and backing plate are set to room temperature T_a .

III. INVERSE SOLUTION OF FRICTION COEFFICIENT

In the present article, the ISM is used to obtain the unknown friction coefficient $\mu(T)$. The ISM used in the present article follows the framework proposed by Maalekian *et al.*^[36] and is slightly modified to deal with the present thermal model. The inverse problem is solved based on the following three rules.

(1) The relative error function S_1 ,

$$S_1 = \int_{t_0}^{t_c} |Y_t - T_t| dt \Big/ \int_{t_0}^{t_c} T_t dt \quad [10]$$

should be smaller than a given threshold tolerance.

(2) For every single time-step, the absolute error function S_2 , which is the difference between the

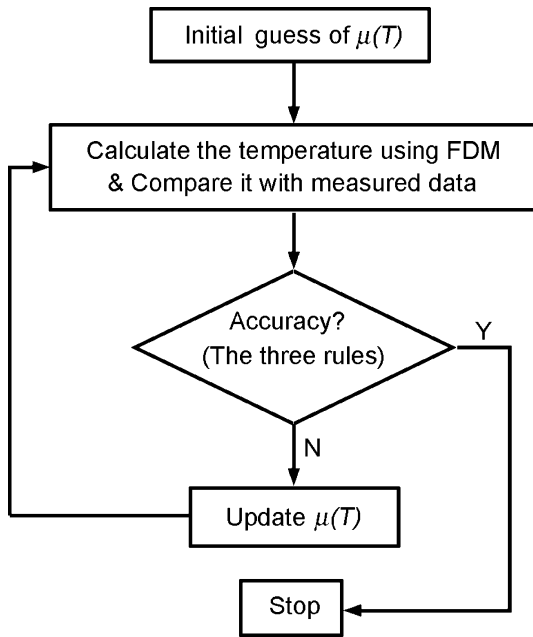


Fig. 2—Slightly modified flow chart for the ISM computation based on Ref. 36.

computed temperature and the measured temperature, should also be smaller than a given threshold tolerance:

$$S_2 = |Y_t - T_t| \quad [11]$$

where $t_0 \leq t \leq t_e$.

- (3) At the melting point of the workpiece, the friction coefficient is negligible. In the present article,

$$\mu(T_{melt}) = 0 \quad [12]$$

is adopted.

The inverse method is used to solve the temperature-dependent friction coefficient $\mu(T)$ by using the measured transient temperature data at point X_0 . For an original guess of $\mu(T)$, the heat generation rate can be calculated by Eq. [2]. Then the transient temperature Y_t at point X_0 of the workpiece can be computed by the finite differential method (FDM) and compared with the measured data T_t . If the three rules are satisfied, the current $\mu(T)$ is admissible. If anyone of the three rules is not satisfied, a correction step is applied to $\mu(T)$ and the preceding computation is repeated. The ISM algorithm can be summarized by the flow chart in Figure 2.

IV. EXPERIMENTS

In the present article, a digital notation for the FSW samples, as suggested by Liu and Ma,^[39] is used, where sample 24-8-1400-200 indicates that the sample is welded by using a shoulder 24 mm in diameter and a pin 8 mm in diameter at a rotation rate of 1400 rpm and an advancing speed of 200 mm/min. For both ISM and predicting computation in this study, the following parameter specification is adopted. FSW of 6061-T651

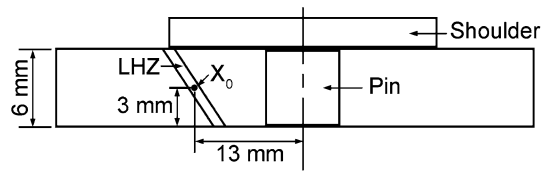


Fig. 3—Illustration of the thermocouple position (point X_0) for sample 24-8-1400-200^[39].

aluminum alloy plates 400 mm in length, 75 mm in width, and 6 mm in thickness is studied. The tool material is M42 high speed tool steel. A tilting angle of 3 deg, axis force of 20 KN,^[31] plunge speed of 10 mm/min, weld length of 360 mm, and a threaded pin are used.

Temperature-dependent density, heat conductivity, and specific heat capacity of the 6061-T651 aluminum alloy, which are taken from Reference 40, are given in the following quadratic polynomials

$$\rho = -3.57 \times 10^{-11}(T - 273)^2 - 1.86 \times 10^{-7}(T - 273) + 2.71 \times 10^{-3} \quad [13a]$$

$$\lambda = -2.59 \times 10^{-7}(T - 273)^2 + 2.08 \times 10^{-4}(T - 273) + 1.74 \times 10^{-1} \quad [13b]$$

$$c = 1.79 \times 10^{-7}(T - 273)^2 + 3.32 \times 10^{-4}(T - 273) + 9.10 \times 10^{-1} \quad [13c]$$

The governing equations and the boundary conditions are solved in a FDM based computer code. The computation and postprocessing are performed on MATLAB.

V. COMPUTED RESULTS

The experiments consist of two steps: first, the ISM computation is used to obtain the friction coefficient; and second, by using the friction coefficient, the transient thermal model is used to predict the temperature and heat generation for FSW.

For the ISM computation, the experimentally measured thermal cycle of sample 24-8-1400-200^[39] is used as input data (T_t). The thermocouple position is shown in Figure 3. For predicting the temperature and heat generation, sample 24-8-900-200 is simulated.

A. ISM Computation

The ISM computed thermal cycle for sample 24-8-1400-200 is shown in Figure 4, as well as the input thermal cycle measured by Liu and Ma^[39] for the ISM computation. For the entire temperature range, good agreement can be observed. Figure 5 depicts the variation of the ISM computed friction coefficient with temperature. For simplifying the subsequent discussion, locally fitted curves, which are linear approximation, are also offered.

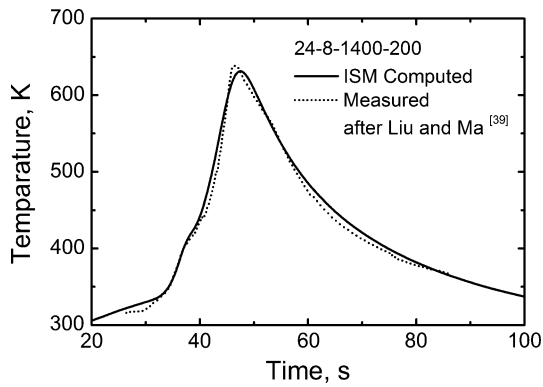


Fig. 4—Measured temperature^[39] at X_0 for inverse computation and the corresponding ISM computed temperature.

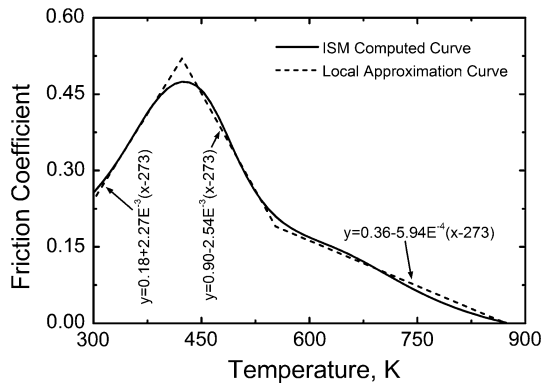


Fig. 5—ISM computed temperature-dependent friction coefficient. Piecewise dash lines denote local approximation curves.

B. Predicting Computation

The present transient thermal model simulates the entire FSW process. The entire FSW process for sample 24-8-900-200 can be divided into six periods, as shown in Figure 6: the first plunge period (period I), from 0 to 29.2 seconds, before the shoulder contacts with the workpiece; the second plunge period (period II), from 29.2 to 36 seconds, after the shoulder contacts with the workpiece; the first dwell period (period III), from 36 to 38 seconds; the weld period (period IV), from 38 to 146 seconds; the second dwell period (period V), from 146 to 148 seconds; and the cooling period (period VI) after 148 seconds. The calculated results are described subsequently.

1. Transient temperature

Dynamic maximum temperature during the FSW process is shown in Figure 6. At the end of the first plunge period, the maximum temperature on the top surface of the workpiece reaches 498 K (225 °C). The dynamic maximum temperature of 736 K (463 °C) is reached at 36.7 seconds, which is a little later after the shoulder completely contacts with the workpiece. At t_4 time the steady maximum temperature of 714 K (441 °C) is reached.

The calculated thermal cycle at the heat-affected zone for sample 24-8-900-200 is compared with the

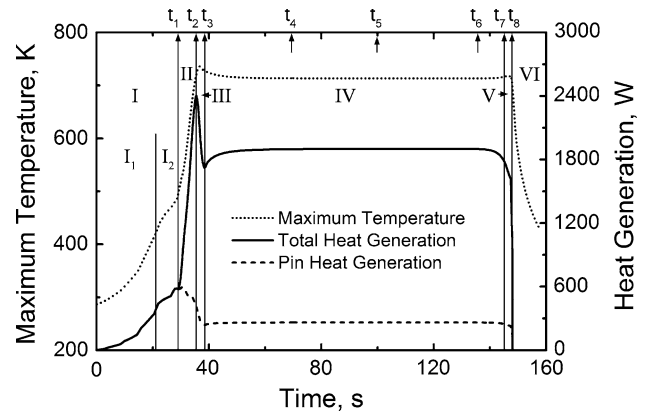


Fig. 6—Predicted dynamic maximum temperature, total heat generation, and pin heat generation for sample 24-8-900-200 with marked time points at the top.

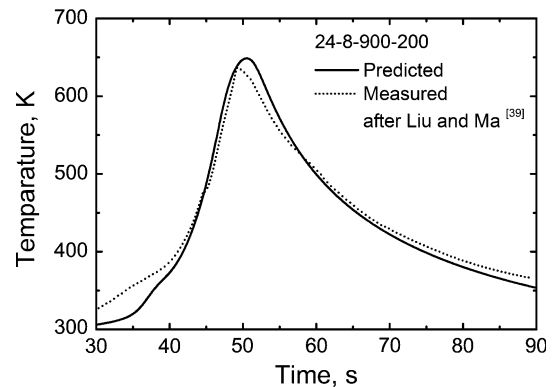


Fig. 7—Comparison between calculated thermal cycle and measured result for sample 24-8-900-200^[39].

experimental data measured by Liu and Ma^[39] in Figure 7. Good agreement is observed. The computed thermal cycle shows a peak temperature of 649 K (376 °C).

Thermal contours on the top and butting surfaces around the tool at the end of each FSW period are shown in Figures 8 and 9, respectively. The black circle in Figure 8 and the black polygonal lines in Figure 9 illustrate the outline of the tool. Two important findings can be observed in these figures. First, for various periods, the density of the isothermal contours in front of the tool is different from that at the rear of the tool. As the tool travels from the original position of 20 mm to the position of 346 mm, the contours are compressed in front of the tool and expanded at the rear of the tool. At the end of the weld, the contours are expanded in front of the tool and compressed at the rear of the tool. Second, the closed contours under the tool are not concentric with the tool outline. The hottest region of the workpiece under the tool is located at the rear of the tool until the tool reaches the position of 346 mm. However, the hottest region moves in front of the tool at the end of the weld, as shown in Figures 8(g) and (h) and 9(g) and (h). Figures 6, 8, and 9 indicate that, for sample 24-8-900-200, the steady-state temperature fields

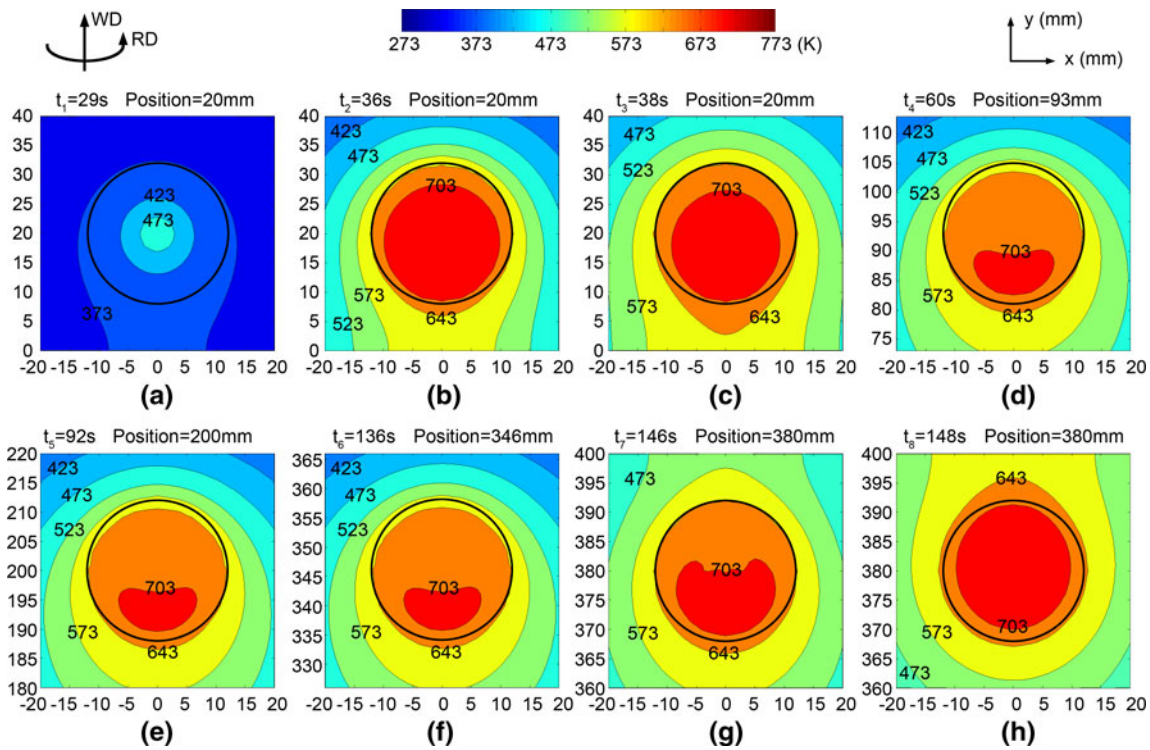


Fig. 8—Temperature contours on the top surface at different times for sample 24-8-900-200. The black circles denote the shoulder outline. The time point settings are shown in Fig. 6.

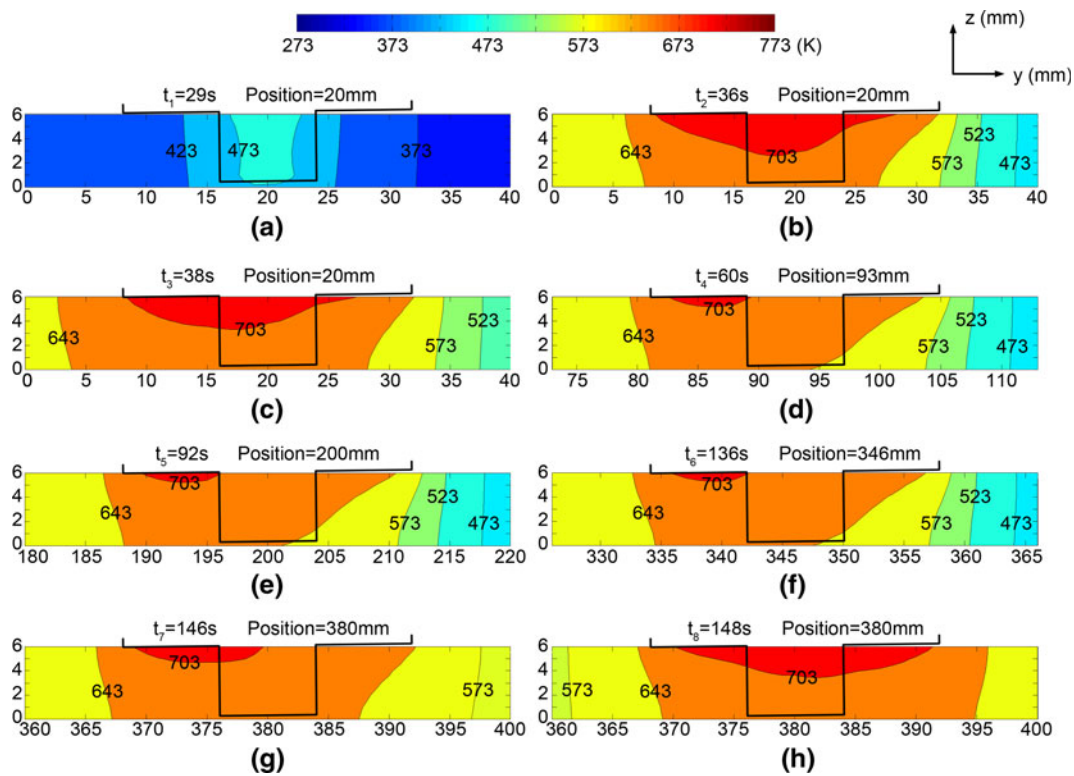


Fig. 9—Temperature contours on the butting surface at different times for sample 24-8-900-200. The black polygonal lines denote the tool outline.

in the weld period are from t_4 60 to t_6 136 seconds, which is from the position of 93 mm to the position of 346 mm in the welding direction.

2. Transient heat generation

Both total heat generation and pin heat generation evolution curves are shown in Figure 6. For different FSW periods, the heat generation shows different values and variation trends. As the tool plunges into the plates, the total heat generation equals the pin heat generation, which rises slowly to 586 W in period I. Then the total heat generation rises sharply until 2400 W in the end of period II. However, the pin heat generation begins to drop in period II. In period III, the total heat generation drops to 1748 W and the pin heat generation decreases to 241 W. At the beginning of period IV, the total heat generation rises slowly until a steady-state total heat generation of 1894 W, defined as Q_{total}^s , is built at time t_4 . The pin heat generation has a similar trend in period IV, and the steady-state pin heat generation is 261 W. At the end of the weld, both total heat generation and pin heat generation decrease and the trend continues in period V until the tool extracts from the workpiece.

VI. DISCUSSION

To critically analyze the accuracy of the present thermal model, we will consider the following: (a) the physically reasonable analysis of the temperature-dependent friction coefficient; (b) the self-consistent analysis of the present thermal model; and (c) the reliability analysis using Sato *et al.*'s weld conditions,^[41] where the measured temperature was reported.

A. Physical Reasonableness Analysis of the Temperature-Dependent Friction Coefficient

In the following part, we will discuss the main potential factors affecting the friction coefficient^[33] during FSW to explore the key friction-affecting factor.

1. Effect of temperature

For FSW of the aluminum alloys, the nugget zone experiences a temperature excursion from room temperature to ~ 0.6 to $\sim 0.9 T_{\text{melt}}$ of the workpiece.^[42] For example, in the present article, the calculated temperature near the tool/workpiece contact area is above 643 K (370 °C) (Figure 9) and the maximum temperature is 714 K (441 °C) (Figure 6) in the steady-state welding for FSW of the 6061Al-T651 (sample 24-8-900-200). Thus, it can be seen that the temperature of the contact area varies in a very large range during the FSW process. This leads to significant changes of the mechanical properties of the workpiece (especially in the nugget zone), the contact state of the tool/workpiece interface,^[33] and in turn the friction coefficient.

The temperature-dependent friction coefficient was observed in previous studies. Reference 43 reported that the sliding friction coefficient for the aluminum/steel friction couple was about 0.25 at room temperature based on dry sliding tests. On the other hand, the

stick friction coefficient value for aluminum was reported to approach 0.5,^[44] when the sliding friction force exceeds the shear yield strength of the workpiece at high temperatures.^[29,40] These facts suggest that the friction coefficient exhibits a strong correlation with temperature.

Further evidence supporting the temperature-dependent friction coefficient comes from Zhang *et al.*'s study.^[45] They measured the friction behavior of the 3003-H18 aluminum alloy at different relative surface velocities and temperatures. It was reported that at room temperature the friction coefficient was 0.274, and it increased to a maximum value of 0.400 at 423 and 473 K (150 and 200 °C). Above 473 K (200 °C), it began to decrease.

In material removal tests, Tao *et al.*^[46] found that the friction coefficient for 6061Al-T6 was also a temperature-dependent value. With 5 deg wedge angles, the friction coefficient raised from about 1.1 at room temperature to about 1.3 at 523 K (250 °C), beyond which it decreased. They explained that as the temperature increased from room temperature, the adherence between the two friction bodies increased until 523 K (250 °C), at which point the adherence reached a maximum value. When the temperature exceeded 523 K (250 °C), the strengthening phase β'' in the 6061Al-T6 dissolved into the α aluminum matrix, which weakened the strength of 6061Al-T6 and reduced the friction coefficient. Note that the friction coefficient values in Tao *et al.*'s study^[46] differ from those in the present study and other studies. This may be attributed to the different experimental/process conditions.

Most recently, Schmidt and Hattel^[7] proposed the concept of the *self-stabilizing effect*, which was responsible for the temperature level below the solidus temperature, and made the heat generation during FSW a result of the process itself. The self-stabilizing effect was stated as follows: *temperature exceeds solidus temperature \rightarrow yield stress of workpiece decreases \rightarrow heat generation reduces \rightarrow temperature reduces \rightarrow yield stress of workpiece recovers.*^[7] This indirectly supports the temperature-dependent friction coefficient. This effect is further developed in the present article and described as the following *chain rule I*:

Temperature of the tool/workpiece interface increases (when the temperature is higher than a limited temperature, i.e., 423 K (150 °C) in the present article) \rightarrow material strength decreases \rightarrow friction coefficient decreases \rightarrow heat generation decreases \rightarrow increment of temperature decreases and its inverse path temperature of the tool/workpiece interface decreases (when the temperature is lower than a limited temperature, i.e., 423 K (150 °C) in the present article) \rightarrow material strength increases \rightarrow friction coefficient increases \rightarrow heat generation increases \rightarrow increment of temperature increases.

Chain rule I shows the relationship between temperature, heat generation, and friction coefficient. This is the key characteristic of the FSW differing from the fusion weld process where the heat input can be precisely controlled, *e.g.*, by setting current and voltage.^[47] Furthermore, Figure 5 suggests that when the temperature exceeds 423 K (150 °C), the variation of the

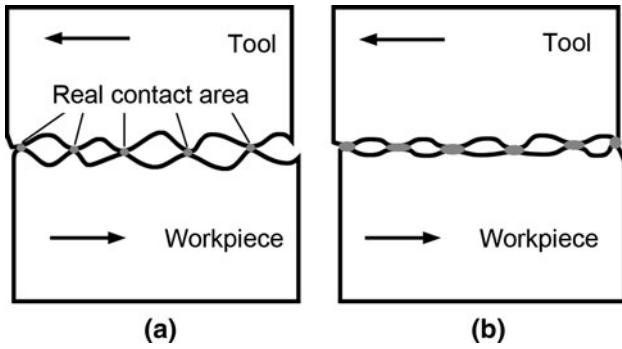


Fig. 10—Illustration of the sliding friction interfaces that may occur in FSW: (a) small part of the apparent contact area is the real friction area,^[34] and (b) increased temperature softens the workpiece and increases the real contact area under the normal pressure.

friction coefficient with temperature may be approximately described by a piecewise linear equation:

$$\mu(T) = \mu_0 - K(T - 273) \quad [14]$$

where $\mu_0 = 0.90$, $K = 2.54 \times 10^{-3}$ for $423 \text{ K} (150^\circ\text{C}) < T \leq 553 \text{ K} (280^\circ\text{C})$, and $\mu_0 = 0.36$, $K = 5.94 \times 10^{-4}$ for $553 \text{ K} (280^\circ\text{C}) < T \leq 873 \text{ K} (600^\circ\text{C})$.

From Eqs. [12] and [14], we can get $\frac{\mu_0}{K} = T_{\text{melt}} - 273$, for $T > 553 \text{ K} (280^\circ\text{C})$. Thus, the friction coefficient becomes zero at the melting point of the workpiece material. This is supported by Schmidt and Hattel's study.^[7] They gave a heat generation model $q = \tau(T)\omega r$, which suggested that the friction stress monotonically decreased with the rising temperature and dropped to zero as the temperature increased up to the melting point. This supports the present work well.

Figure 5 also suggests that in the range from room temperature to $423 \text{ K} (150^\circ\text{C})$, the friction coefficient is approximately proportional to the temperature. According to Tao *et al.*'s study^[46] with the explanation depicted in Figure 10, we can deduce the *chain rule II with positive feedback mechanism* as follows:

Temperature of the tool/workpiece interface increases (when the temperature level is lower than $423 \text{ K} (150^\circ\text{C})$ in the present study) \rightarrow the adherence between the tool and the workpiece material increases \rightarrow friction coefficient increases \rightarrow heat generation increases \rightarrow increment of temperature increases.

Such a deduction still needs more evidence to prove its reasonability. The *positive feedback mechanism* may be approximately described by

$$\mu(T) = 0.18 + 2.27 \times 10^{-3}(T - 273), \quad \text{for } 273 \text{ K} (0^\circ\text{C}) < T < 423 \text{ K} (150^\circ\text{C}) \quad [15]$$

The influence of the chain rule I with negative feedback mechanism and chain rule II with positive feedback mechanism on the final heat generation and temperature will be discussed in Section VI-B.

2. Other potential friction-affecting factors

Contact geometry (*i.e.*, macroscale mating of shapes and surface roughness) of the contact components^[33] is also a potential friction-affecting factor. For the FSW

process, the contact components are the tool (including the shoulder and the pin) and the workpiece. In the present study and a companion article,^[37] the tools with different diameters were all made from M42 high speed tool steel with the same shape, while the workpiece is a 6061Al-T6. It can be easily seen that the contact geometry of the tool and the workpiece is the almost the same.

For FSW, the relative motion (*i.e.*, magnitude of relative surface velocity) between the tool and the workpiece, a potential friction-affecting factor,^[33] can be expressed by $u = \frac{2\pi\omega}{60}r + \frac{v}{60}\sin\theta$. In most cases, $\frac{2\pi\omega}{60}r \gg \frac{v}{60}\sin\theta$; thus, $u \approx \frac{2\pi\omega}{60}r$, from which we know that the relative motion between the tool and the workpiece is controlled by the rotation rate. In the present study and a companion article,^[37] the rotation rate is in the range of 900 to 1400 rpm, the increase of which is less than 2 times. Furthermore, Zhang *et al.*^[45] measured the friction coefficients of 3003-H18 Al under different sliding speeds. They found that as the sliding speed increased from 0.80 to 800 mm/s (*i.e.*, three orders of magnitude), the friction coefficient remained at the same level of 0.27. Based on these facts, it is possible to deduce that the effect of relative motion between the tool and the workpiece on the friction coefficient is small.

According to Peel *et al.*'s study,^[31] with the same shoulder plunge depth, which is also the case in the present article and a companion article,^[37] the applied force increased by 15, 12, and 35 pct, respectively, for FSW of 6082Al-T6 with increasing the weld pitch (a parameter resulting from dividing the advancing speed by the rotation rate) from 0.18 to 0.54, for FSW of 5083Al with increasing the weld pitch from 0.18 to 0.54, and for FSW of dissimilar 6082Al-5083Al with increasing the weld pitch from 0.12 to 1.07. Recently, Atharifar *et al.*^[48] reported that as the advancing speed decreased from 150 to 30 mm/min at a constant rotation rate of 31.4 rad/s, the axis force increased from 8.2 to 9.5 kN. With increasing the rotation rate from 31.4 to 125.6 rad/s at a constant advancing speed of 150 mm/min, the axis force increased from 8.2 to 18.0 kN. These experimental results revealed that the applied force in FSW varied with the welding parameters, but the variation was still in the same magnitude.

Another potential friction-affecting factor is the contact compliance (*i.e.*, sliding and sticking friction conditions). By considering both sliding and sticking friction conditions, the friction heat generation rate can be expressed by

$$q = (1 - \delta)\mu_c p \left(\frac{2\pi\omega}{60}r + \frac{v}{60}\sin\theta \right) + \delta\eta\tau \left(\frac{2\pi\omega}{60}r + \frac{v}{60}\sin\theta \right) \quad [16]$$

The term $\mu_c p$ is the Coulombic friction stress, while τ is the shear strength. When δ is 0, the heat generation is described only by the first term of Eq. [16], indicating a full sliding condition, *i.e.*, Coulombic friction. When δ is 1, the heat generation is described only by the second item, which is a full sticking condition; *i.e.*, a full

plasticity at the frictional interface occurs. However, it is difficult to determine the δ function in FSW. Thus, far-reaching approximations are used to describe the δ function. For example, Maalekian *et al.*^[34] assumed that δ was a function of temperature with a friction conversion time of 0.1 seconds. Nandan *et al.*^[13,14] assumed that δ was a function of the relative velocity between the tool and the workpiece. In the present article, we follow Maalekian *et al.*'s^[34] framework. In this case, δ and τ in Eq. [16] are temperature-dependent functions. Then Eq. [16] can be rewritten as

$$q = \left[(1 - \delta)\mu_c + \delta\eta\frac{\tau}{p} \right] p \left(\frac{2\pi\omega}{60}r + \frac{v}{60}\sin\theta \right) \quad [17]$$

If we define a function

$$\tilde{\mu} = (1 - \delta)\mu_c + \delta\eta\frac{\tau}{p} \quad [18]$$

it can be seen that $\tilde{\mu}$ is a function completely dependent on the temperature. Further, Eq. [17] can be simplified to $q = \tilde{\mu}(T)p\left(\frac{2\pi\omega}{60}r + \frac{v}{60}\sin\theta\right)$, which has the same form as Eq. [2]. Therefore, the temperature-dependent friction coefficient can be used to describe both sliding and sticking conditions based on the assumption that the slip fraction is a function of temperature.

To summarize, temperature is the key factor affecting the friction coefficient in FSW, while other potential friction-affecting factors such as contact geometry (*i.e.*, macroscale mating of shapes and surface roughness), relative motion (*i.e.*, magnitude of relative surface velocity), and applied force (*i.e.*, magnitude of normal force) have small effects on the friction coefficient for the FSW process. For simplifying the computation, an approximation is adopted in the present article that the friction coefficient is only dependent on the temperature. The potential friction-affecting factor, the contact compliance (*i.e.*, sliding and sticking friction conditions), is embedded in the present heat generation rate formula.

B. Self-Consistency and Computed Heat Generation

To further prove the validity of the present thermal model, the self-consistency of the model is examined by the dynamic heat generation results from the present thermal model. The friction coefficient function, which is the core element in the present thermal model, can be examined indirectly.

The characteristics of the computed dynamic heat generation curve depicted in Figure 6 are in good agreement with the experimental results reported by Schmidt *et al.*^[29] Since the temperature point of 423 K (150 °C) is an inflection point of the friction coefficient-temperature curve, period I can be subdivided into two subperiods, periods I₁ and I₂, based on the 423 K (150 °C) temperature point on the maximum temperature curve, as shown in Figure 6. The total amount of heat generation in period I is relatively small, because the heat is only generated on the pin/workpiece interface. In period I₁, the temperature in the friction interface is lower than 423 K (150 °C). According to the previous discussion, the friction coefficient in period

I₁ is controlled by the positive feedback mechanism, resulting in faster and faster increasing of the friction coefficient and in turn the heat generation and the temperature, as depicted in period I₁ of Figure 6. When the maximum temperature in the friction interface exceeds the inflection point of 423 K (150 °C), the friction coefficient on the pin/workpiece interface is controlled by the negative feedback mechanism. This results in the reduction in the friction coefficient and in turn the heat generation rate q during period I₂. However, the area of the pin/workpiece interface increases in this period, which increases the heat generation and compensates for the decrease in the friction coefficient due to the negative feedback mechanism. Therefore, the heat generation and temperature during period I₂ still increases but with a lower increasing rate compared to period I₁, as shown in Figure 6.

When the shoulder comes in contact with the workpiece in period II, the contact area rises quickly and therefore the heat generation increases sharply. As the heat generation increases sharply to 2400 W, the maximum temperature rises quickly from 498 K to 731 K (225 °C to 458 °C). The negative feedback mechanism indicates that the temperature increasing rate will not keep its original value due to the decrease in the friction coefficient, which means that the temperature level is below the solidus temperature of the alloy. This is also the reason that the pin heat generation drops in period II, whereas the total heat generation rises quickly due to the increase in the contact area.

The drop in the axis force during the dwell period should be responsible for the quick decrease in the heat generation in period III, as reported by Schmidt *et al.*^[29] and Cavaliere *et al.*^[49]

At the beginning of period IV, the weld period, the value of the heat generation rises slightly. This behavior may be explained in Figure 11. We plot both the friction coefficient-temperature curve and the temperature position along the welding line in Figure 11(a). The temperature ahead of the tool is lower than that on the tool/workpiece interface, as shown in Figure 8(c). With the tool moving ahead, the tool encounters the thermal contours with lower temperature values, which decreases the temperature on the tool/workpiece interface. According to the negative feedback mechanism, decreasing of temperature increases the friction coefficient, and in turn increases the heat generation, which compensates the temperature. This behavior cycles many times until an equilibrium state is established at time t_4 , which may be summarized by this path $1 \rightarrow 2 \rightarrow 3 \rightarrow 1' \rightarrow 2' \rightarrow 3' \rightarrow 1'' \rightarrow 2'' \rightarrow 3'' \rightarrow \dots \rightarrow \text{equilibrium point}$, as shown in Figure 11(b).

With the tool reaching the end of the weld, the isothermal contours are expanded in front of the tool and compressed behind it, as shown in Figures 8(g) and (h). The reason for this is that heat transported at a slower rate to the surrounding through the workpiece/surrounding interface, while heat transferred rapidly through the workpiece behind the tool. Since the temperature in the front of the tool is higher than that at the rear of the tool, according to the negative

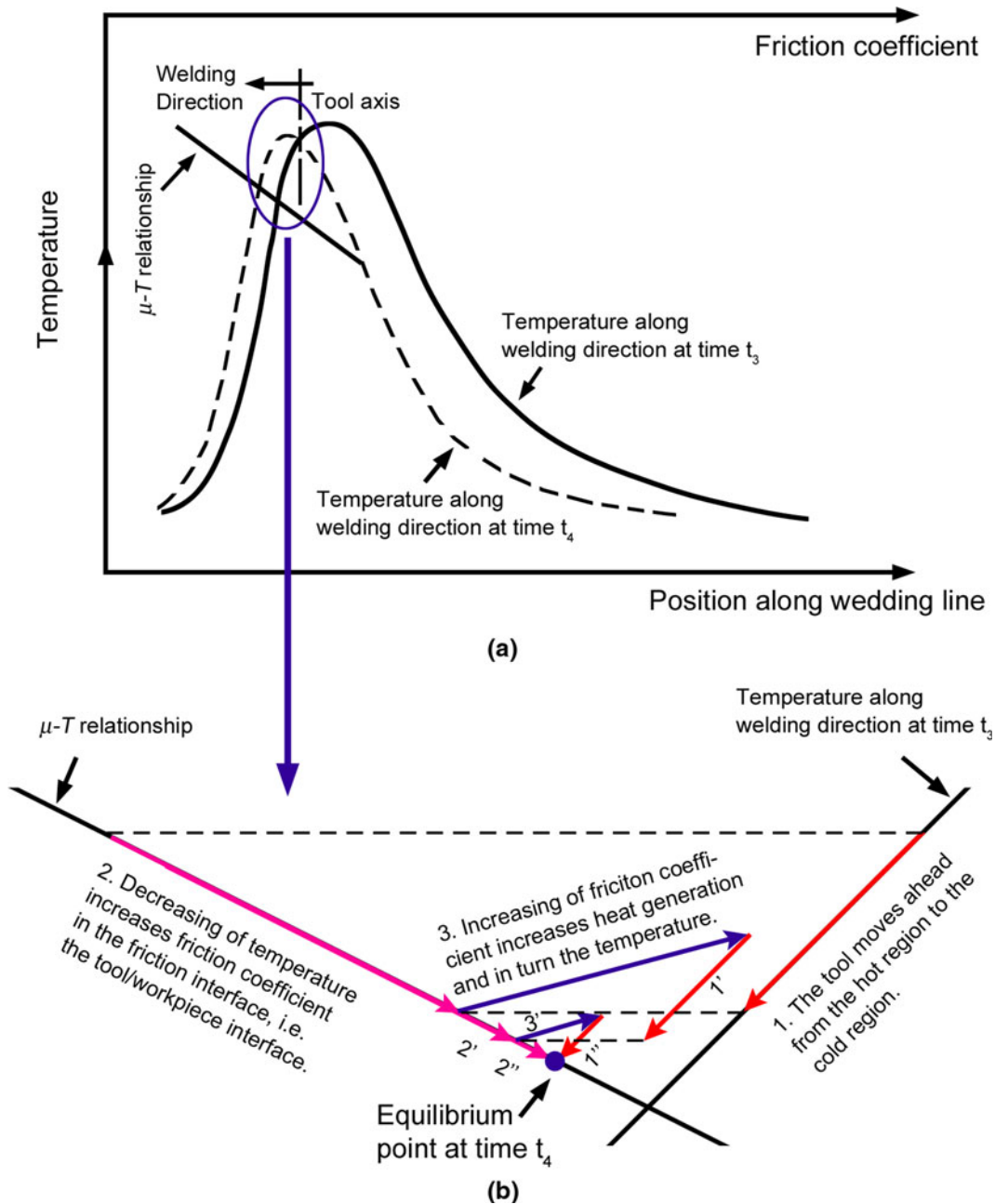


Fig. 11—Illustration of the processes to establish the FSW equilibrium state in FSW period IV: (a) the friction-temperature relation and the temperature-position relation along the welding line, and (b) the detailed steps depicting how the FSW reaches its equilibrium state with the tool moving ahead.

feedback mechanism, the heat generation decreases at the end of the weld period when the tool moves ahead, as shown in Figure 6. In period V, the high-temperature region expands, resulting in the decrease in the heat generation. With the tool extracts from the workpiece, the heat generation decreases to zero.

In conclusion, the characteristics of computed heat generation including dynamic data and steady-state data, and the pin heat generation fraction under various weld conditions, can be well explained by the chain rules.

C. Reliability Test

To evaluate the relative achievements of the present thermal model, the weld conditions reported by Sato *et al.*,^[41] where thermal cycles for FSW 6063Al-T5 were experimentally measured using a thermocouple placed at the bottom of the butt line, were applied to the weld parameters set in the present model. The thermophysical properties of the 6063Al-T5 actually refer to those of 6061Al-T6, a similar alloy with slightly lower alloying element contents. Computed maximum temperatures at

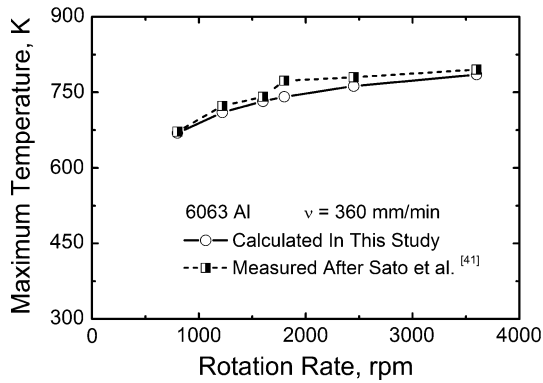


Fig. 12—Comparison between computed and measured^[41] maximum temperatures.

the bottom surface of the SZ agree well with the measured results^[41] for different rotation rates, as depicted in Figure 12. This suggests that in spite of the approximation of the friction coefficient, the present thermal model is robust to predict the temperature under a wide range of welding conditions.

VII. CONCLUSIONS

1. A transient thermal model for the entire FSW process is established based on the temperature-dependent friction coefficient, which can be obtained by ISM. The transient thermal model can be used for predicting temperature and heat generation of FSW. The predicted results correspond well with the experimentally measured results reported by Liu and Ma^[39] and Sato *et al.*^[41]
2. The relation between temperature, friction coefficient, and heat generation for FSW can be summarized by a phenomenological approach, which consists of the chain rule I with negative feedback mechanism that dominates at the middle and high temperatures and the chain rule II with positive feedback mechanism that dominates at the low temperatures. Furthermore, the FSW process reaches an equilibrium state under the control of the negative feedback mechanism, indicating that the FSW is a self-stabilizing process with respect to computed temperature and heat generation.

ACKNOWLEDGMENTS

The authors gratefully acknowledge the support of (a) the National Outstanding Young Scientist Foundation of China under Grant No. 50525103 and (b) the Hundred Talents Program of the Chinese Academy of Sciences.

NOMENCLATURE

c	heat capacity ($\text{J K}^{-1} \text{g}^{-1}$)
F_z	axis force (N)
h_b	heat-transfer coefficient ($\text{W mm}^{-2} \text{K}^{-1}$)

h_p	pin length (mm)
h_t	heat-transfer coefficient ($\text{W mm}^{-2} \text{K}^{-1}$)
K	curve fitting slope
k	thermal conductivity ($\text{W mm}^{-1} \text{K}^{-1}$)
l, w, h	length, width, and thickness of workpiece (mm)
p	pressure (Pa)
p_q	pressure at pin/workpiece interface (Pa)
p_s	pressure at shoulder/ workpiece interface (Pa)
$Q_p, Q_s, Q_{\text{total}}$	pin, shoulder, and total heat generation (W)
q	heat generation rate (J mm^{-3})
R_p, R_s	pin, shoulder radius (mm)
r	radius (mm)
T	temperature (K)
T_a	room temperature (K)
T_t	reference temperature at time t (K)
t	time (s)
t_0	start time for inverse computation (s)
t_e	end time for inverse computation (s)
t_{total}	total time of FSW process (s)
u	relative speed between the tool and the workpiece
v	advancing speed (mm min^{-1})
v_W	velocity of the workpiece (mm s^{-1})
v_T	velocity of the tool (mm s^{-1})
x, y, z	coordinate axes
Y_t	computed temperature at time t (K)
∇	gradient operator, $\nabla \equiv \frac{\partial}{\partial x} + \frac{\partial}{\partial y} + \frac{\partial}{\partial z}$
δ	slip fraction, $\delta \equiv v_W/v_T$
ε	emissivity
$\dot{\varepsilon}$	strain rate (s^{-1})
η	mechanical efficiency
μ	comprehensive friction coefficient
μ_0	curve fitting intercept
μ_c	Coulombic friction coefficient
λ	thermal conductivity ($\text{W mm}^{-1} \text{K}^{-1}$)
ρ	density (g mm^{-3})
σ	Stefan–Boltzmann constant ($\text{J s}^{-1} \text{mm}^{-2} \text{K}^{-4}$)
ω	rotation rate (rpm)
π	Pi

REFERENCES

1. W.M. Thomas, E.D. Nicholas, J.C. Needham, M.G. Church, P. Templesmith, and C. Dawes: International Patent Application No. PCT/GB92/02203 and GB Patent Application No. 9125978.9, 1991.
2. R.S. Mishra and Z.Y. Ma: *Mater. Sci. Eng. R*, 2005, vol. 50, pp. 1–78.
3. C.G. Rhodes, M.W. Mahoney, W.H. Bingel, R.A. Spurling, and C.C. Bampton: *Scripta Mater.*, 1997, vol. 36, pp. 69–75.
4. G. Liu, L.E. Murr, C.S. Niou, J.C. McClure, and F.R. Vega: *Scripta Mater.*, 1997, vol. 37, pp. 355–61.
5. L.E. Murr, G. Liu, and J.C. McClure: *J. Mater. Sci.*, 1998, vol. 33, pp. 1243–51.
6. Y.S. Sato, H. Kokawa, M. Enmoto, and S. Jogan: *Metall. Mater. Trans. A*, 1999, vol. 30, pp. 2429–37.
7. H.B. Schmidt and J.H. Hattel: *Scripta Mater.*, 2008, vol. 58, pp. 332–37.
8. S. Xu, X. Deng, and A.P. Reynolds: *Sci. Technol. Weld. Join.*, 2001, vol. 6, pp. 191–93.

9. H. Schmidt and J. Hattel: *Model. Simul. Mater. Sci. Eng.*, 2005, vol. 13, pp. 77–93.
10. Q.Z. Zhang, L.W. Zhang, W.W. Liu, X.G. Zhang, W.H. Zhu, and S. Qu: *Sci. Technol. Weld. Join.*, 2006, vol. 11, pp. 737–43.
11. G. Buffa, J. Hua, R. Shivpuri, and L. Fratini: *Mater. Sci. Eng. A*, 2006, vol. 419, pp. 389–96.
12. Z. Zhang and H.W. Zhang: *Int. J. Adv. Manuf. Technol.*, 2008, vol. 37, pp. 279–93.
13. R. Nandan, G.G. Roy, and T. DebRoy: *Metall. Mater. Trans. A*, 2006, vol. 37A, pp. 1247–59.
14. R. Nandan, G.G. Roy, T.J. Lienert, and T. DebRoy: *Acta Mater.*, 2007, vol. 55, pp. 883–95.
15. A. Arora, R. Nandan, A.P. Reynolds, and T. DebRoy: *Scripta Mater.*, 2009, vol. 60, pp. 13–16.
16. A.P. Reynolds, W. Tang, Z. Khandkar, J.A. Khan, and K. Lindner: *Sci. Technol. Weld. Join.*, 2005, vol. 10, pp. 190–99.
17. D. Santiago, S. Urquiza, G. Lombera, and L. Vedia: *Soldagem Insp. São Paulo.*, 2009, vol. 14, pp. 248–56.
18. S. Guerdoux and L. Fourment: *Model. Simul. Mater. Sci. Eng.*, 2009, vol. 17, pp. 075001–32.
19. C. Hamilton, A. Sommers, and S. Dymek: *Int. J. Mach. Tools Manuf.*, 2009, vol. 49, pp. 230–38.
20. S. Zhang, Y.L. Liu, and J.T. Chen: *Int. J. Adv. Manuf. Technol.*, 2009, vol. 45, pp. 889–95.
21. G. Buffa and L. Fratini: *Sci. Technol. Weld. Join.*, 2009, vol. 14, pp. 239–46.
22. A. Bastier, M.H. Maitournam, K. Dang, and F. Roger: *Sci. Technol. Weld. Join.*, 2006, vol. 11, pp. 278–88.
23. H.N.B. Schmidt and J. Hattel: *Int. J. Offshore Polar. Eng.*, 2004, vol. 14, pp. 296–304.
24. Y.J. Chao and X. Qi: *Proc. 1st Int. Symp. on Friction Stir Welding*, TWI, Thousand Oaks, CA, June 1999, pp. 31–38.
25. Ø. Frigaard, Ø. Grong, and O.T. Midling: *Metall. Mater. Trans. A*, 2001, vol. 32A, pp. 1189–98.
26. M. Song and R. Kovacevic: *Int. J. Mach. Tools Manuf.*, 2003, vol. 43, pp. 605–15.
27. C. Chen and R. Kovacevic: *Mach. Tools Manuf.*, 2003, vol. 43, pp. 1319–26.
28. M.Z.H. Khandkar, J.A. Khan, and A.P. Reynolds: *Sci. Technol. Weld. Join.*, 2003, vol. 8, pp. 165–74.
29. H. Schmidt, J. Hattel, and J. Wert: *Model. Simul. Mater. Sci. Eng.*, 2004, vol. 12, pp. 143–57.
30. H. Schmidt and J. Hattel: *Sci. Technol. Weld. Join.*, 2005, vol. 10, pp. 176–86.
31. M.J. Peel, A. Steuwer, P.J. Withers, T. Dickerson, Q. Shi, and H. Shercliff: *Metall. Mater. Trans. A*, 2006, vol. 37A, pp. 2183–93.
32. A. Anders, Larsen, M. Bendsøe, J. Hattel, and H. Schmidt: *Struct. Multidisc. Optim.*, 2009, vol. 38, pp. 289–99.
33. *ASM Handbook, Friction, Lubrication, and Wear Technology*, P.J. Blau, ed., ASM INTERNATIONAL, Materials Park, OH, 1992, vol. 18, pp. 27–69.
34. M. Maalekian, E. Kozeschnik, H.P. Brantner, and H. Cerjak: *Acta Mater.*, 2008, vol. 56, pp. 2843–55.
35. A. Sluzalec: *Int. J. Mech. Sci.*, 1990, vol. 32, pp. 467–78.
36. M. Maalekian, E. Kozeschnik, H.P. Brantner, and H. Cerjak: in *Mathematical Modelling of Weld Phenomena 8*, H. Cerjak, H.K.D.H. Bhadeshia, and E. Kozeschnik, eds., Verlag der Technischen Universität Graz, Graz, 2007, pp. 881–90.
37. X.X. Zhang, B.L. Xiao, and Z.Y. Ma: *Metall. Mater. Trans. A*. DOI:10.1007/s11661-011-0730-z.
38. M.N. Ozisik: *Heat Conduction*, John Wiley & Sons Inc., Canada, 1993, pp. 1–36.
39. F.C. Liu and Z.Y. Ma: *Metall. Mater. Trans. A*, 2008, vol. 39A, pp. 2378–88.
40. *Recommended Values of Thermophysical Properties for Selected Commercial Alloys*, C.M. Kenneth, ed., Woodhead Publishing Ltd., Abington, England, 2002, pp. 64–67.
41. Y.S. Sato, M. Urat, and H. Kokawa: *Metall. Mater. Trans. A*, 2002, vol. 33A, pp. 625–35.
42. W.J. Arbegast and P.J. Hartley: *Proc. 5th Int. Conf. on Trends in Welding Research*, Pine Mountain, GA, June 1–5, 1998, pp. 541–46.
43. *Friction Data Guide: An Engineering Study of Coefficient of Friction of Materials and Coatings*, Slide-Chart Presentation from General Magnaplate Corp., Linden, NJ, 1988.
44. H.S. Kong and M.F. Ashby: *Engineering Department Report*, Cambridge University, Cambridge, United Kingdom, 1991.
45. C.B. Zhang, X.J. Zhu, and L.J. Li: *87th FABTECH International and AWS Welding Show Professional Program*, Atlanta, GA, 2006, pp. 151–56.
46. Z.H. Tao, M.R. Lovell, and J.C. Yang: *Wear*, 2004, vol. 256, pp. 664–70.
47. *ASM Specialty Handbook*, J.R. Davis, ed., ASM INTERNATIONAL, Materials Park, OH, 1993, p. 392.
48. H. Atharifar, D.C. Lin, and R. Kovacevic: *J. Mater. Eng. Perform.*, 2009, vol. 18, pp. 339–50.
49. P. Cavaliere, G. Campanile, F. Panella, and A. Squillace: *J. Mater. Process. Technol.*, 2006, vol. 180, pp. 263–70.